Frontiers of Information Technology & Electronic Engineering
www.jzus.zju.edu.cn; engineering.cae.cn; www.springerlink.com
ISSN 2095-9184 (print); ISSN 2095-9230 (online)
E-mail: jzus@zju.edu.cn

Review:

Terahertz time-domain spectroscopy and micro-cavity components for probing samples: a review*

Lin CHEN[†1,2,3], Deng-gao LIAO[1], Xu-guang GUO[1,2], Jia-yu ZHAO[1,2], Yi-ming ZHU[†1,2,3], Song-lin ZHUANG[†‡1,2]

[1]*Shanghai Key Lab of Modern Optical System, University of Shanghai for Science and Technology, Shanghai 200093, China*
[2]*Shanghai Cooperation Innovation Centre of Terahertz Spectroscopy and Imaging Technology, Shanghai 200093, China*
[3]*Cooperative Innovation Center of Terahertz Science, University of Electronic Science and Technology, Chengdu 611731, China*
[†]E-mail: linchen@usst.edu.cn; ymzhu@usst.edu.cn; slzhuang@yahoo.com

Received Oct. 11, 2018; Revision accepted Mar. 11, 2019; Crosschecked May 13, 2019

Abstract: We give a brief review of the developments in terahertz time-domain spectroscopy (THz-TDS) systems and micro-cavity components for probing samples in the University of Shanghai for Science and Technology. The broadband terahertz (THz) radiation sources based on GaAs m-i-n diodes have been investigated by applying high electric fields. Then, the free space THz-TDS and fiber-coupled THz-TDS systems produced in our lab and their applications in drug/cancer detection are introduced in detail. To further improve the signal-to-noise ratio (SNR) and enhance sensitivity, we introduce three general micro-cavity approaches to achieve tiny-volume sample detection, summarizing our previous results about their characteristics, performance, and potential applications.

Key words: Terahertz (THz) time-domain spectroscopy; Micro-cavity; Metal holes array; Waveguide cavities; Spoof localized surface plasmons (LSPs)
https://doi.org/10.1631/FITEE.1800633 **CLC number:** O441

1 Introduction

With the development and blossoming of applications of terahertz (THz) technology, huge potential applications in different fields have been found and realized (Libon et al., 2000; Ferguson et al., 2002; Siegel, 2002; Wu et al., 2003; Biber et al., 2004; He et al., 2012; Zang et al., 2015), such as biological imaging, material detection, next generation communication, medical spectroscopy, and pollution diagnostics (Federici and Moeller, 2010; Wang et al., 2014, 2015). Recently, THz-TDS has been attracting wide interest. THz-TDS uses short pulses of broadband THz radiation excited by a femtosecond laser and the effective time sampling technique to acquire spectral information in the THz band. This generation method has been built from an attempt by Auston in the 1980s (Auston DN et al., 1984; Fattinger and Grischkowsky, 1988). Historically, freely propagating THz signals are detected under photoconductive antennas (PCAs) (Auston DH et al., 1984; DeFonzo et al., 1987) or far infrared interferometric techniques using incoherent detectors such as bolometers (Jones, 1947; Johnson et al., 1980). However, developments in the THz field have been restricted by the need for efficient broadband THz sources (Hangyo et al., 2006). In recent years, THz science and technology

‡ Corresponding author
* Project supported by the National Key R&D Program of China (No. 2018YFF01013003), the Program of Shanghai Pujiang Program, China (No. 17PJD028), the National Natural Science Foundation of China (Nos. 61671302, 61601291, and 61722111), the Shuguang Program supported by the Shanghai Education Development Foundation and Shanghai Municipal Education Commission, China (No. 18SG44), the Key Scientific and Technological Project of Science and Technology Commission of Shanghai Municipality, China (No. 15DZ0500102), the Shanghai Leading Talent, China (No. 2016-019), and the Young Yangtse Rive Scholar, China (No. Q2016212)
ORCID: Lin CHEN, http://orcid.org/0000-0002-6848-5257

has seen rapid development in China. The THz laboratory in the University of Shanghai for Science and Technology (USST), as a specially established THz research laboratory, has developed the systems and technology for THz spectroscopy. The laboratory has realized THz broadband sources, conventional THz-TDS and fiber-coupled THz-TDS systems for probing the unique spectral signatures of samples in the THz range. However, traditional THz-TDS are heavily challenged when the amount of samples is tiny, as is often the case in biological or dangerous samples. In this review, first, a broadband THz-TDS system designed and built in USST is introduced in detail. In this system, we use a GaAs m-i-n diode as the THz emitter (Zhu et al., 2008a), whose spectral range can reach 4 THz. The scan speed of the system can be 10 scans/s. A typical setup using the electro-optic (EO) sampling THz detection technique (Ferguson and Zhang, 2002) is also introduced in detail. Then, a compact and portable fiber-coupled THz-TDS system has also been successfully produced. Main features of this system are as follows: scanning speed: 0.1 s/scan; SNR<70 dB; spectrum width>3.5 THz; volume<50 cm×40 cm×30 cm; weight: ~5 kg. Based on these THz measurement platforms, a typical application for THz spectroscopy is to identify anti-diabetic drugs and 2-hydroxyglutaric acid disodium salt (2HG) (Du et al., 2012; Chen WQ et al., 2017). Finally, to overcome the disadvantage of THz-TDS and increase detection sensitivity, three typical high quality (Q) micro-cavity devices are investigated: subwavelength metal holes array (Chen et al., 2013a), waveguide cavities, and whisper gallery (WG) mode based on spoof localized surface plasmons (LSPs) (Chen L et al., 2017). Their performance and applications are also analyzed. The results in this review indicate that although THz spectroscopy can identify the unique footprints of some spectral molecular structures, high Q micro-cavity devices can solve tiny-volume sample probing with high signal-to-noise ratios (SNR) and sensitivity.

2 THz-TDS based on GaAs m-i-n diode

2.1 Broadband THz source in GaAs m-i-n diode

Traditionally, THz radiation from a PCA uses the low-temperature growth of gallium arsenide due to the annihilation of photo-generated carriers in the defect, resulting in dramatic changes in photocurrent and generation of THz electromagnetic waves (Katzenellenbogen and Grischkowsky, 1991). The THz wave generated by this method is generally only about 2.5 THz when the output power is above 1% of the peak power. THz generation can also be achieved by Cherenkov difference frequency generation in a lithium niobate waveguide (Staus et al., 2008; Bodrov et al., 2009), which has high nonlinearity/damage threshold/transparency and small multi-photon absorption. Using the Cherenkov radiation method (Auston DN et al., 1984), phase matching is automatically satisfied at a certain angle with respect to the laser path during propagation. Moreover, as radiation in a lateral direction, the trace of the THz wave inside the lithium niobate is short, resulting in low absorption. The THz generation by Cherenkov difference frequency generation in a lithium niobate waveguide enables extension of the frequency range up to 6 THz (Consolino et al., 2012; Carbajo et al., 2015).

Here, we propose pure intrinsic gallium arsenide as the core layer of the device, which is able to withstand ultra-high electric fields (up to 300 kV/cm), making the electrons able to be accelerated. According to Maxwell's equation, the THz intensity radiated from the device is proportional to the carrier acceleration, and the THz source radiation spectrum width can be extended to ~4 THz with a conversion efficiency higher than 1.5%.

Fig. 1a shows the broadband GaAs m-i-n geometry. The thickness of the intrinsic GaAs layer is 1 μm. We deposited/annealed AuGeNi on the back side of the sample to achieve ohmic contact (Zhao et al., 2002). Another semitransparent NiCr Schottky film contact was fabricated/deposited on the front side. Thus, a direct current electric field can be applied to the intrinsic GaAs layer. The size of the source is 1.5 mm×1 mm.

The performance of this THz source is measured by the free space EO sampling technique, which can obtain time-domain waveforms related to THz amplitude emitted from the samples (Wu and Zhang, 1997a; Planken et al., 2001). The EO detector is a ZnTe crystal with a thickness of 1 μm (spectral bandwidth ~4 THz) (Wu and Zhang, 1997b; Leitenstorfer et al., 1999).

Fig. 2 shows the temporal waveforms of the THz amplitude emitted from the m-i-n diode.

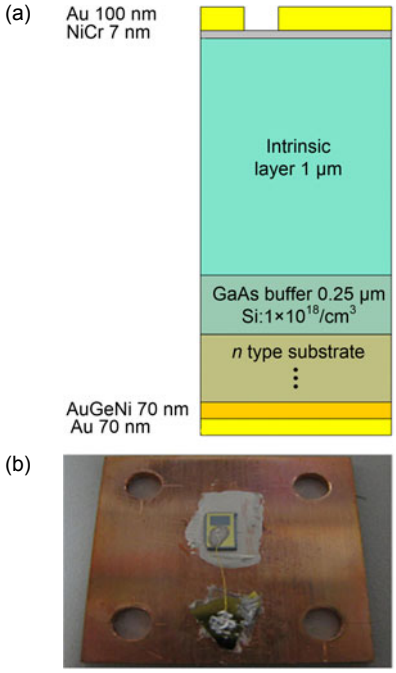

Fig. 1 Cross sections of the GaAs m-i-n diode (a) and image of the sample mount (b)

The m-i-n diode had a metal-intrinsic-n type semiconductor (m-i-n) geometry with a 1-μm thick intrinsic GaAs layer. Ohmic contacts were fabricated by depositing and annealing AuGeNi alloy on the back side of the samples. A semi-transparent NiCr Schottky film was deposited on the surfaces to apply DC electric fields to the intrinsic GaAs layer

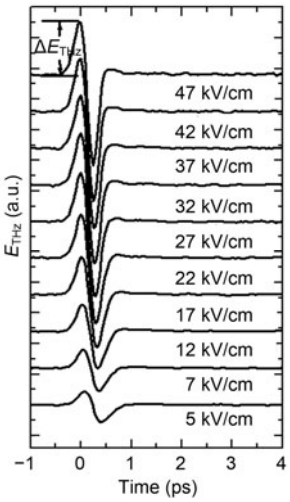

Fig. 2 Time-domain waveforms of THz amplitude emitted from the m-i-n diode

The acceleration of electrons in bulk GaAs occurs when the electrical field is added. The initial positive part of the THz pulse corresponds to ballistic acceleration of electrons in the Γ valley and the subsequent sudden dip of the THz pulse expresses deceleration due to intervalley transfer from the Γ valley to the satellite valleys at 300 K. Reprinted from Zhu et al. (2008b), Copyright 2008, with permission from *Applied Physics Letters*

According to the Maxwell equations, the THz electric field (E_{THz}) in Fig. 2 is given by (Zhu et al., 2008b)

$$E_{\mathrm{THz}} \propto \frac{\partial v}{\partial t}. \tag{1}$$

From Fig. 2, the leading edge of THz waveform comes from the duration of the femtosecond pulses and the spectral bandwidth of the ZnTe detector. The E_{THz} illustrates features of an initial positive peak and a subsequent negative dip due to the velocity overshoot (Leitenstorfer et al., 2000). The initial positive peak and the subsequent negative dip have been regarded as electron acceleration in the Γ valley and electron deceleration from inter-valley transfer, respectively. By increasing the electric field, E_{THz} increases more abruptly. The THz emission spectra extend up to ~4 THz (Fig. 3). As we can see, the bandwidth of the spectrum of the emitted THz trace of the LTG-GaAs based PCA (FAST-SCAN THZ SPECTROSCOPY KIT) is 2.5 THz (https://ekspla.com/). However, in Fig. 3, the bandwidth of THz power of the GaAs antenna is larger than 4 THz, and the peak frequency is around 1.5 THz. Note that the ultrahigh voltage can be added on the intrinsic layer of GaAs. According to Maxwell's theory, $E_{\mathrm{THz}} \propto \mu(E\partial n/\partial t + n\partial E/\partial t)$, where μ is the carrier mobility, E is the applied electric field, and n is the average carrier density in the sample generated by the femtosecond pump laser pulses. For the intrinsic GaAs material, the number of carriers after the laser irradiated is almost a constant, and the effect of $\mu E\partial n/\partial t$ can be ignored. Large mobility and acceleration of electrons result in large THz power.

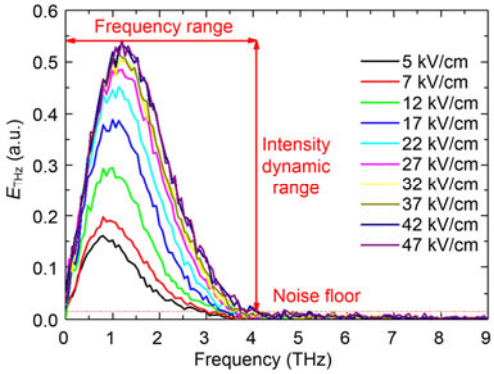

Fig. 3 THz spectra obtained from time-domain THz traces

The noise floor (0.01), intensity dynamic range (0.53), and frequency range (4 THz) have also been listed. References to color refer to the online version of this figure

2.2 THz-TDS systems and their applications

THz-TDS provides a powerful tool for determination of many materials at THz frequencies. Fig. 4 shows the typical THz-TDS setup with EO sampling measurements. The femtosecond laser pulse is split into two parts: a strong pump light and a weak probe light. The pump light illuminates the GaAs m-i-n diode and radiates the THz beam. Then, the THz beam is radiated on an EO ZnTe crystal. A delay line is mechanically moved to vary the time-domain delay between the THz/probe pulses. The E_{THz} can be measured by scanning the time delay. The principle of this sampling method is that THz signals are obtained by sampling and using the femtosecond probe pulse. To increase the SNR, the pump light passes through a chopper with ~kHz modulation. The THz signal can be extracted by a lock-in amplifier.

Based on the above principle, the THz Laboratory in USST has produced the THz drug analyzer (Fig. 5). With the femtosecond laser, and a computer together with our home-made software, this spectrometer can equip an ultrafast optical lab for extending into the research field of THz spectroscopy with high cut-off frequency (3 THz). The THz drug analyzer can acquire THz time-domain waveforms within 100 ps. After Fourier transformation, the system has a spectral resolution of 0.01 THz (10 GHz).

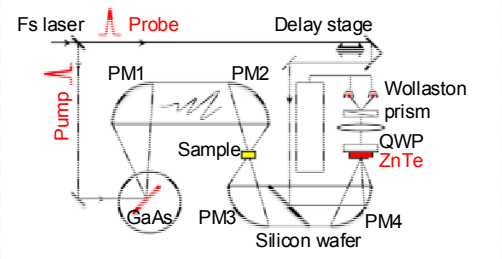

Fig. 4 Experimental setup for free space EO sampling

Fig. 5 THz time-domain spectrometer developed in USST

As an example, anti-diabetic drugs have been measured by this system.

Figs. 6a and 6b show the THz time-domain waveforms and the Fourier transformation of gliquidone, glipizide, gliclazide, glimepiride, respectively. Their absorptions from 0.3 to 2.0 THz are plotted in Fig. 7. Strong absorption peaks at ~1.37 THz have been found for gliquidone, glipizide, gliclazide, and glimepiride. This absorption peak agrees with the vibration peak of the sulfonylurea group, indicating that the absorption peak (1.37 THz) in all the sulfonylureas is attributed to the vibration of the sulfonylurea group.

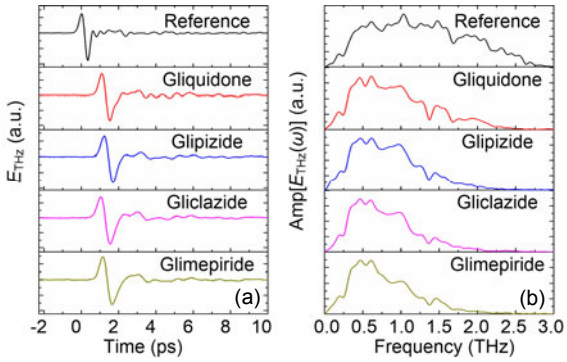

Fig. 6 Free space (reference) and anti-diabetic drugs in the THz time domain (a) and THz frequency domain (b)
Reprinted from Du et al. (2012), Copyright 2012, with permission from *Applied Physics Letters*

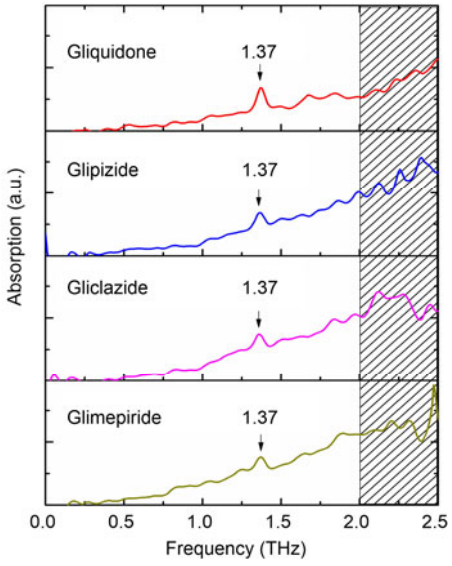

Fig. 7 Experimental THz absorption spectra of gliquidone, glipizide, gliclazide, and glimepiride
Reprinted from Du et al. (2012), Copyright 2012, with permission from *Applied Physics Letters*

To make the system flexible and portable, the fiber-coupled THz-TDS has also been developed independently. It consists of three main parts: the main unit (volume 40 cm×40 cm×20 cm, 220-V mains connected all the way), hand-held probe (connected to the host via a 1-m optical cable), computer (connected to 220-V mains and the host via USB cable, used as host control). The THz spectrometer occupies about 1 m^2 of the table area, and the probe can move in a circular area with a radius of 1 m. The THz spectrometer housing needs to be grounded. The system components are displayed in Fig. 8.

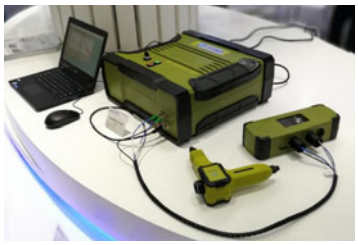

Fig. 8 Main components to the fiber coupled time-domain spectrometer in operation

The probe contains a THz transmitter and receiver. The THz wave emitted by the THz transmitter is transmitted or reflected by the sample. The THz wave carries the specific information of the sample and is measured by the THz receiver and converted into an analog time-domain signal and transmitted to the host. Use of the m-i-n diode THz source comes with independent intellectual property rights of the USST. It has the characteristics of a wide spectrum range and good stability of radiation signals. Main features of this system are as follows: scanning speed, 0.1 s/scan; SNR<70 dB; spectrum width>3.5 THz; volume<50 cm×40 cm×30 cm; weight: ~5 kg.

Next, we take the 2HG as an example. The THz absorption spectra of L-2HG and D-2HG are shown in Fig. 9. Their THz absorption spectra show small different characteristics, which can be used to identify L-2HG and D-2HG.

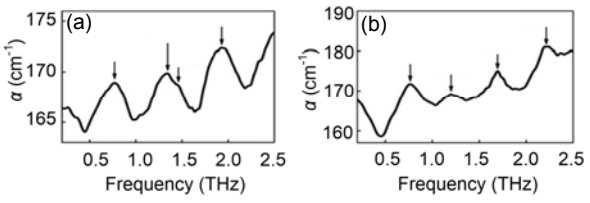

Fig. 9 Absorption spectra of L-2HG (a) and D-2HG (b)
Reprinted from Chen WQ et al. (2017), Copyright 2017, with permission from Springer Nature

3 THz micro-cavity devices and their applications in sensing

The technology of THz-TDS for biosensing is used to identify the fingerprint spectrum or extract the complex refractive index and absorption coefficient from spectroscopy. The challenge in THz-TDS is that samples should have enough volume to be sensed (Pupeza et al., 2007). Then they can interact sufficiently with the radiation. Samples with a tiny volume have a weak interaction in conventional spectroscopy configurations. The transmitted wave modifies less when passing through it. Such small modification cannot distinguish the sample from the reference sample. The criterion that the sample cannot be distinguished from the reference is (O'Hara et al., 2008; Withayachumnankul et al., 2014)

$$\frac{\omega l}{c}\Delta n(\omega) < \sqrt{\frac{2}{N}}S(\omega), \tag{2}$$

where l is the sample thickness, $S(\omega)$ is the standard phase deviation of the reference spectra, N is the number of sample measurements, and Δn is the refractive index difference between sample and reference. In addition, there are some other challenges (dramatically enhanced THz power or random fluctuations of the generated and detected THz waves induced by inherent instabilities of the ultrafast laser) which prevent improving SNR and a reduction of the noise floor (Theuer et al., 2010a, 2010b). This challenge of THz-TDS is the main motivation for the description of new sensing methods. In the following, we will present several micro-cavity resonator methods to improve SNR and enhance sensitivity (Lu et al., 2011).

3.1 Metallic photonic crystal

Early in 1998, it was found that a subwavelength metallic hole array structure exhibited an extraordinary optical transmission feature at a certain wavelength (Ebbesen et al., 1998). This unique phenomenon was interpreted quickly by surface plasmon (SP) theory; i.e., the beam passing through the holes is carried by exciting SPs (Ghaemi et al., 1998). Miyamaru and Hangyo (2004) transferred this concept to the THz range. Here such extraordinary optical transmission was achieved by a metallic photonic

crystal (PC) with a thickness of the subwavelength scale (Miyamaru et al., 2006). The momentum matching condition between SPs and in-plane incident waves in a metallic PC is sensitive to a change in the dielectric on the surface and can be implemented for THz sensing (Qu et al., 2004). In this section, we discuss the performance of this extraordinary optical transmission and its application in sensing. The photo and geometrical structure of an aluminum PC slab are shown in Fig. 10. A triangular array with circular air holes is arranged on the PC slab with 250-μm thickness. The area of the sample is 50 mm×50 mm. The size of a single hole is as follows: 0.7 mm diameter, a pitch of a hexagonal lattice s=1.13 mm. The number of holes is larger than 5000 to avoid the finite size effect (Xu et al., 2013a). In the THz range, an SP at a metal interface is weakly localized and most of the energy of the surface plasmon polariton modes comes from electromagnetic waves localized at the air side. The designed structure acts as a 2D grating that can add momentum to incident light in both the in-plane and out-of-plane directions.

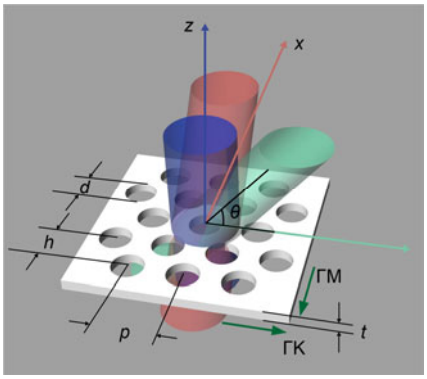

Fig. 10 A photo of the aluminum PC plate
The proposed metallic PC slab consisted of a triangle array of circle air holes on a t=250-μm thick, 50×50-mm rectangular aluminum plate. The circle air holes had a diameter of d=0.7 mm, and they are arranged on a hexagonal lattice with a pitch of p=1.13 mm. A collimated p-polarized (along the x axis) THz wave was irradiated on the metallic PC

The extraordinary optical transmission was measured using the THz-TDS system mentioned above. A signal without the sample was used as a reference for our measurements.

Fig. 11 shows the results at normal incidence. The time-domain signal experienced obvious attenuating oscillation, indicating strong interaction between the THz waves and the weak surface plasmon polaritons on the designed surface. Their Fourier transformation (frequency-domain spectra) is shown in Fig. 11b. There exists a resonant peak (0.265 THz), resulting from the fundamental mode of metallic PC. Here the periodical structure is constructed on the metal surface, so the dispersion curve can satisfy the coupling of the incident electromagnetic wave with the surface mode.

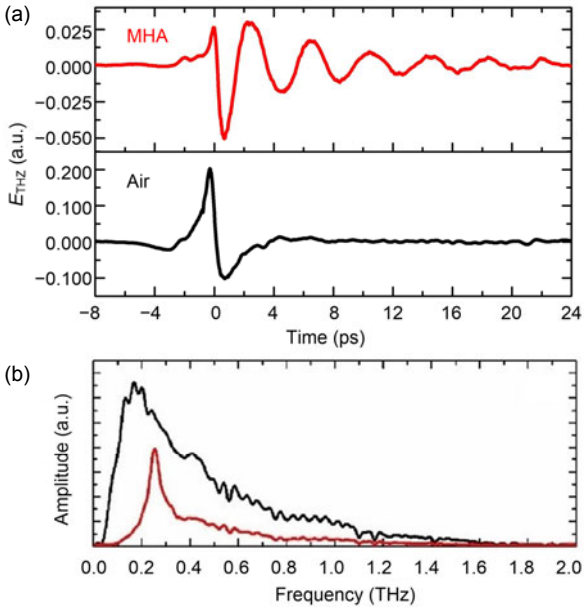

Fig. 11 Incident and transmitted THz waveform of MHAs at normal incidence in the time domain (a) and corresponding spectra in the frequency domain (b)
References to color refer to the online version of this figure. Reprinted from Chen et al. (2013a), Copyright 2013, with permission from Springer Nature

Next, we discuss the detection of monohydric alcohol solvents using a metallic PC. As is well known, alcohols have widespread applications as solvents in chemistry and the pharmaceutical industry and are regarded as a model for investigation of hydrogen bonded networks. The chemical structures of methanol, ethanol, 1-propanol, and 1-butanol are shown in Fig. 12. These structures are composed of different numbers of hydroxyl groups (-OH) with carbon atoms of the alkyl group. The frequency-dependent absorption coefficients (α) and refractive indices (n) of the monohydric alcohols gradually decline from the methanol to 1-butanol (Yomogida et al., 2010; Markelz, 2008). The THz absorption spectra of the monohydric alcohols present a monotonic rising feature and the absorption intensities decrease

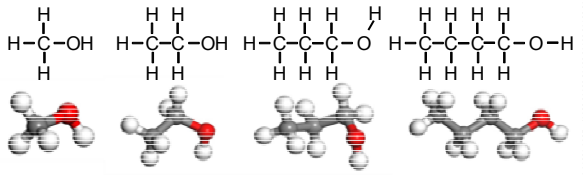

Fig. 12 Left to right: methanol, ethanol, 1-propanol, and 1-butanol

The positions of hydroxyl groups and structures of carbon chains are different from each other and affect the formation of hydrogen bonds in the liquid. This leads to the differences among the absorption coefficients and refractive indices of monohydric alcohols

with increasing length of the alkyl group. The THz absorption intensity always depends on the polarity of the liquid. The greater the polarity, the stronger the absorption in the THz range (Su, 2014). Also, a lot of research has been done on liquids such as alcohol series, and particularly on the complex permittivity of alcohols (Bertero et al., 2011). Here, we introduced the metallic PC to act as a new type of sensor. The sheet metal with micro-holes array can identify different monohydric alcohol solvents to the shift of resonant peaks in the frequency domain. This can be more easily recognized by the TDS system.

In the experiment, methanol (>99.5%), ethanol (>99.7%), 1-propanol (>99%), and 1-butanol (>99.5%) were obtained from the Shanghai Sinopharm Chemical Reagent Co., Ltd. The metallic PC was placed in the middle of a quartz case box composed of two parallel, 0.4-mm spaced windows. The array was immersed in the liquid samples and the transmission spectra was obtained by THz-TDS. The monohydric alcohols in the cell without the array were measured as the reference. The transmission is defined as $|t(\omega)|=|E_{out}(\omega)/E_{in}(\omega)|$, where ω is an angular frequency, and E_{out} (ω) and $E_{in}(\omega)$ are the frequency-dependent amplitudes of the THz pulses transmitted through the sample and reference, respectively (Dorney et al., 2001).

The monohydric alcohols have different resonance frequencies from each other (Fig. 13). With the increase of the length of the alkyl group, the resonance frequencies show blueshift, resulting from the decrease of the refractive index. In addition, the transmission increases with the increase of the length of the alkyl group. This is because of the decrease of the absorption coefficient.

Compared to the traditional THz-TDS method, the sheet metal with micro-hole array can change the

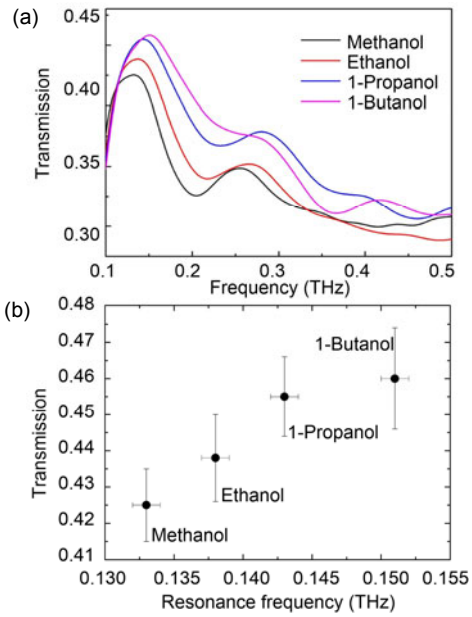

Fig. 13 Measured transmission through metal holes array immersed in monohydric alcohols (a) and transmission and resonance frequencies of monohydric alcohols (b)

References to color refer to the online version of this figure

slight difference of absorptions to the shift of resonant peaks in the frequency domain, and this can be more easily and obviously recognized by the THz-TDS system. It is a potential approach for distinguishing the class or species of chemicals. Further experimental and theoretical results demonstrate that the resonant peak of excitation of surface waves splits into two when it transmits to the arrays off-normally (Chen et al., 2013b).

3.2 Parallel plate waveguide cavities

The limitation of a metallic PC for sensing is its semi-open geometry, which is not suitable for flow monitoring. We describe a THz parallel-plate waveguide (PPWG) with a resonator to solve this problem. The PPWG is analogous to metal-dielectric-metal structures in the visible region (Chen et al., 2007). Mendis et al. (2009) studied a resonant cavity in one metallic plate through adding a stub (groove) across the plate. The device detects the existence of the sample by changing its refractive index to the induction of the guiding mode. A transverse electric (TE_1) mode is used to excite the cavity mode.

The single cavity in PPWG shows a high Q resonant feature in the transmission spectrum. Here, we report an observation of an electromagnetically

induced transparency (EIT)-like appearance in PPWG with two cavities, and the relationship between the deviated position of the cavities and the transmission features was analyzed. The two cavities have identical geometry (Fig. 14). We find that the EIT-like effect found here is the result of resonant hybridization caused by changes in the coupling strength of the top and bottom cavities (Chen et al., 2013c). We also find that the phase shift between two grooves is another key factor in achieving EIT. The resonance dip at low frequency shows a high Q feature. Actually, a plasmonic analogue of electromagnetic induced transparency has also been reported by taking dissimilar (different depth) cavities on two plates while L could remain zero (Huang et al., 2011).

As shown in Fig. 14, the system includes two aluminum plates, each of which has a micro fabrication rectangle groove with the same size of 470-μm width and 420-μm depth. The symmetrical and asymmetrical configurations are achieved by changing the bottom cavity movement length L from 0 to 300 μm. S indicates the gap of the waveguide. The THz-TDS system with the spectrum resolution of 4.58 GHz is used. The gap between two plates, S, is fixed at 650 μm. The PPWG without any cavity acts as reference.

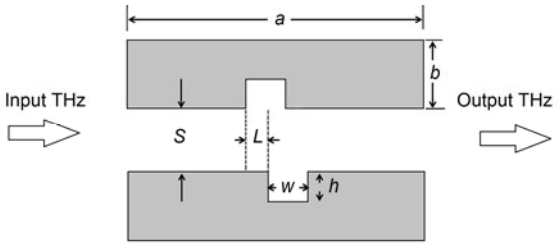

Fig. 14 A general view of PPWG with two cavities
All cavities have identical geometry with width w=470 μm and depth h=420 μm. S, length of the plates; L, shifting length between two grooves. THz radiation is polarized parallel to the plates to excite TE modes

Fig. 15 shows the power transmission with several shifts L. For the symmetric case (L=0 μm), one symmetric dip is found at 0.417 THz. For L=100 μm, a new dip at 0.354 THz occurs. When the shift is increased to 200 μm, the lower resonant frequency exhibits blue shift and the high resonant dip red shift. A transparent window at ~0.36 THz is an EIT-like profile. When the shift is further increased (L= 300 μm), two resonance frequencies get closer and the transmission window becomes narrow and low. The experimental data fits well with numerical calculations in Fig. 15.

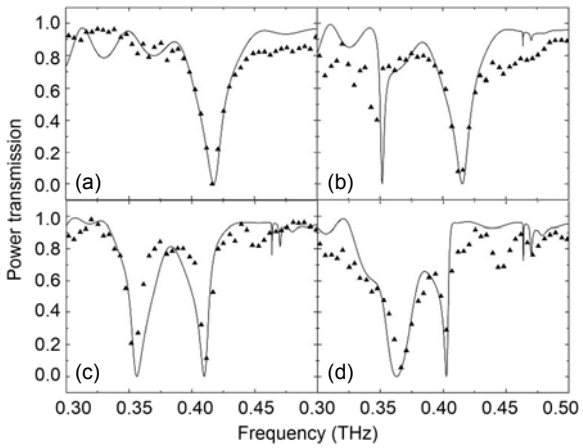

Fig. 15 Power transmission of waveguide cavities system
Solid line: simulation results; dash line and dots: experimental results. (a), (b), (c), and (d) stand for L=0, 100, 200, and 300 μm, respectively

The influence of the gap S is also investigated (Chen et al., 2013c). Here, we set S to 610, 670, 740, and 780 μm, respectively, and these were used to study the characteristics of the EIT. Fig. 16 shows the power transmission with different S. The spectra show obvious EIT phenomena when S varies from 610 to 670 μm. When S is increased to 740 and 780 μm, the symmetric dip degenerates as in Figs. 16c and 16d. The measurement results agree well with the simulation ones (Chen et al., 2014b).

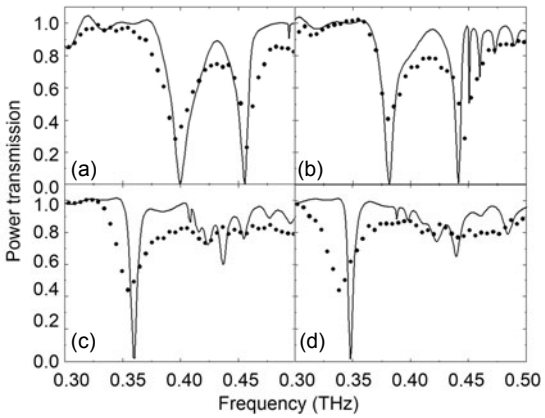

Fig. 16 Experimental spectra with several gaps
Solid line: simulation results; dots: experimental results. (a), (b), (c), and (d) stand for S=610, 670, 740, and 780 μm, respectively. Reprinted from Chen et al. (2013c), Copyright 2013, with permission from *Applied Physics Letters*

Fig. 17 shows the transmission map by changing frequency and waveguide gap (1/*S*). 1/*S* of 1.64, 1.49, 1.35, and 1.28 mm^{-1} represent *S* of 610, 670, 740, and 780 μm in the experiment, respectively. With a fixed moving length *L* (200 μm), as the symmetric resonant wavelength is less than *S*, the electromagnetic wave propagates along a "zigzag line" and acts as a guided wave. The cavities produce little influence on the transmission. Here the increase of *S* converts the Fabry-Perot resonance into a guided wave. Since the EIT transparent peak between two resonances comes from the destructive interference of symmetric and asymmetric resonances, as the transition of symmetric Fabry-Perot resonance takes place, this interference is broken and an on-to-off EIT peak modulation can be achieved in this process.

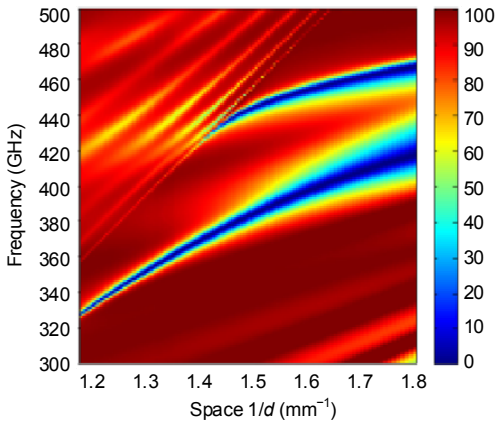

Fig. 17 Transmission map with different *S* (*L*=200 μm)
Reprinted from Chen et al. (2013c), Copyright 2013, with permission from *Applied Physics Letters*

Finally, we show some numerical simulation taking into account different samples and a fixed configuration of the parameters *L* (50 μm) and *S* (650 μm). The principle of the proposed structure as a microfluidic sensor is based on the response of the resonant frequency (asymmetrical mode) to the presence of a sample filling the bottom grooves.

The transmission spectra are numerically calculated using the finite element method (FEM) of COMSOL Multiphysics. Fig. 18 plots the resonance frequency shift for the various samples (the refractive index *n* changes from 1 to 1.3). As we can see, there is a significant red-shift in the transmission dip as the refractive index increases. The sensitivity can achieve 141.43 GHz/RIU. In Fig. 18, it is interesting that the asymmetry induced by refractive index difference in two grooves (see electric field patterns in Fig. 19) can increase the full-width at half-maximum (FWHM) of the resonance dip, resulting in a low *Q* feature.

Next, we evaluate the figure of merit (FOM) for PPWG. The value of FOM can be calculated by FOM=*S*/FWHM, where *S* is the sensitivity and can be defined as the ratio of resonance frequency variation δf to the change in the refractive index of sample δn. FWHM can be determined by calculating the full width at half maximum of the resonance peak/dip. The FOM with respect to the resonance frequency (corresponding to different materials) is shown in

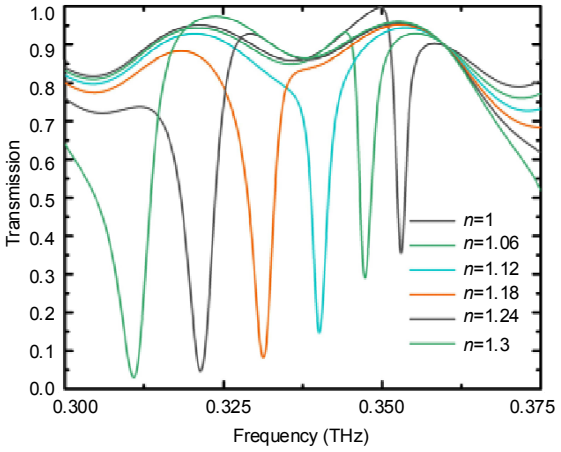

Fig. 18 Transmission with different refractive indices for different frequencies around lower resonance dip
The sample is filled into the cavity embedded in the bottom plate. References to color refer to the online version of this figure

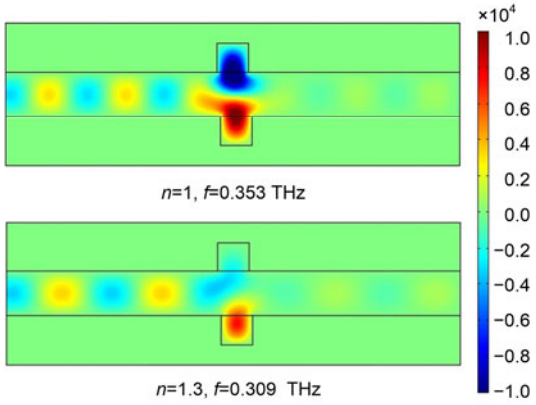

Fig. 19 Simulated electric field patterns for asymmetrical mode at resonance
The refractive index difference of samples in top and bottom grooves leads to another asymmetry, which decreases the energy of the asymmetrical mode, resulting in large FWHM of the resonance dip. References to color refer to the online version of this figure

Fig. 20. The changes of FOM with different frequencies originally come from the FWHM of a different resonance dip. The higher the asymmetry (induced by different samples in two grooves) is, the broader the FWHM is, and the higher the FOM is.

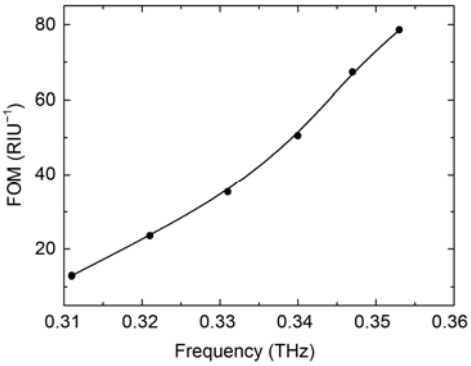

Fig. 20 FOM of the proposed PPWG cavities with L=50 μm and d=650 μm

3.3 Whisper gallery mode micro-cavity induced by spoof localized surface plasmons

PPWG is a bulk platform that is difficult to integrate. Here we introduce an on-chip WG mode micro-cavity induced by spoof localized surface plasmons (LSPs). This is easily integrated. LSPs are usually excited around the particles of nano scale in the visible/near infrared regions. When the frequency shifts to a lower range, metals at these frequencies show high conduction properties, which causes weak interaction. Instead, a periodic textured metallic disk structure is designed to support spoof LSPs at lower frequencies (Por et al., 2012; Shen and Cui, 2014). Such spoof LSPs show WG mode characteristics, which benefit biosensing by exciting multipolar resonances of the hybrid materials, exhibiting high Q values. We investigate the transmission properties of a mixed spoof LSPs structure which consisted of one closed corrugated metallic disk (CMD) and one C-shaped resonator (CSR) structure (Chen L et al., 2017). Fig. 21 (inset) depicts the schematic of the closed CMD and CSR hybrid structure. The angle of the CSR θ is 60°. The inner radii and width of the CSR are R_c=160 μm and w=10 μm, respectively. This means the gap between disk and cap is 10 μm. Fig. 21 shows that obvious multipolar resonances (noted as C1–C5) can be observed theoretically and most of these resonances (C1–C4) are observed experimentally.

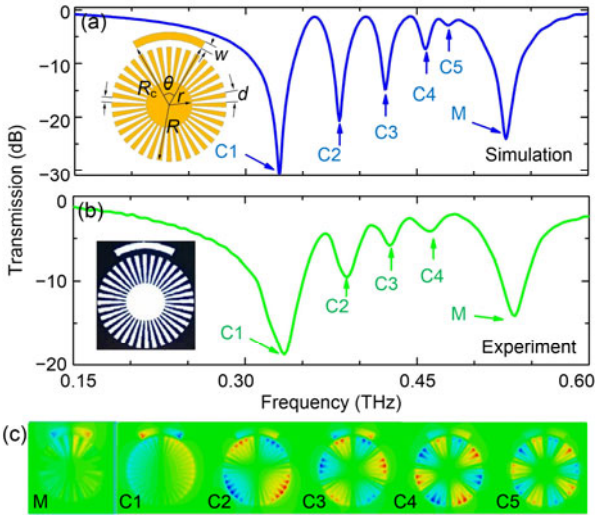

Fig. 21 Theoretical (a) and experimental (b) transmission spectra of cap coupled corrugated texturing closed disk; (c) electric field of multipolar resonances shown as dipole (C1), quadrupole (C2), hexapole (C3), octopole (C4), and decapole (C5) modes

The bright LSP mode supported by single CSR structure results in the resonance (M). The angle of the C-shaped resonator θ is 60°. The inner radii and width of the CSR are R_c=160 μm and w=10 μm, respectively. The gap between disk and cap is 10 μm. The terahertz wave with electric field parallel to the CSR arc illuminates the sample at normal incidence. References to color refer to the online version of this figure. Reprinted from Chen et al. (2016), Copyright 2016, with permission from Springer Nature

The resonance (noted as M) is caused by the bright LSPs excited by CSR. The electric fields corresponding to dips C1–C5 are plotted in Fig. 21c. The CSR is resonant as an LSP mode M, and the disk exhibits multipolar modes, which are consistent with the spoof LSPs modes of a disk. The dark multipole modes from closed CMD are excited by the LSP produced at the CSR. In our system, there is only one dark disk and the dark multiple resonances are induced to be resonant as multipolar modes with spoof LSPs.

The highest-order resonances of spoof LSPs approximate the corresponding asymptote frequencies of LSP. Then, theoretically multipolar resonance can be excited as its resonance frequency is lower than the asymptote frequency in the dispersion curve. However, the resonance frequency of CSR plays an important role in exciting multipolar resonance. If the resonance frequency of CSR is far away from the

asymptote frequency of the structure, high-order resonances can hardly be efficiently excited. While the resonance frequency of CSR overlaps the asymptote frequency of structure, there is interaction between spoof LSP modes and the CSR mode. According to Fig. 21, the highest-order dipole is decapolar. Because the intensity of the highest-order spoof LSPs is weaker when the spoof LSP resonance frequency is near the asymptote frequency, such a highest-order resonance can hardly be observed because of the additional loss from polyimide loss and the fabrication error.

In addition, we propose the geometry of defective CMD with outer radius R=150 μm, inner radius r=60 μm, number of radical metallic grooves N=36, periodicity d=2πR/N, air-filled ratio α=a/d=0.4, 22-μm thick mylar substrate, thickness of the aluminum film t=200 nm, period of the unit cell 360 μm, and defective angle θ=14° (Fig. 22). The wave is incident with E-field polarized perpendicular to the defect. We use conventional lithography to fabricate the defective CMD. The meta-atom array chip has a size of 10 mm×10 mm. A blank mylar identical to the one on which the defective CMDs were fabricated was used as a reference (Chen L et al., 2017).

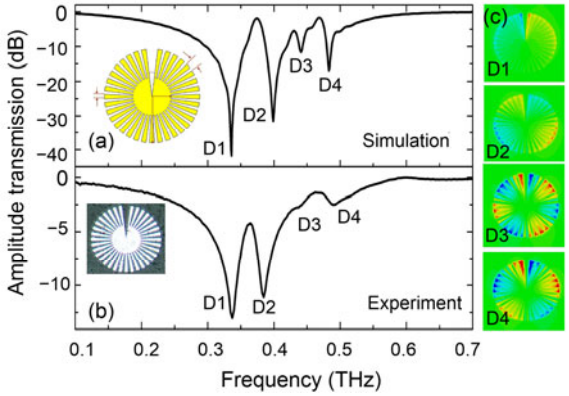

Fig. 22 Theoretical (a) and experimental (b) transmission spectra of defective CMD with θ=14°; (c) electric field of modes D1, D2, D3, and D4 with defective angle θ=14°

The inset depict shows schematics and microscopic image of the defective CMD with r=60 μm, R=150 μm, N=36, d=2πR/N, a=0.4d, θ=14°. The thicknesses of mylar substrate and aluminum film are 22 and 200 nm, respectively. The period of the unit cell is 360 μm. The THz wave with E-field polarized perpendicular to the defective wedge-shaped slice normally transmits through the sample. Reprinted from Chen L et al. (2017), Copyright 2017, with permission from John Wiley & Sons

The sample is measured using a confocal photoconductive-based 8f THz TDS system (Grischkowsky et al., 1990). Fig. 22 shows the transmission spectra results and electric field maps at di- (D1), quadru- (D2), hexa- (D3), and decapole (D4) resonance modes. The excitation of dark multipolar resonance results from the existence of the bright dipole mode from the wedge defect excited by the incident wave. It is interesting to see how the change of angle of defect dark θ influences the dark Fano resonances. Fig. 23 shows the transmission with the increase of angle of defect 14°, 34°, and 54°. We can see that first, the resonance D3 (D4) becomes weaker with the increase of angle of defect because the polar of resonance D3 (D4) near the defective slice edge becomes small and the distortion of the electric field of hexa- (octo-) polar Fano modes has generally deteriorated. In contrast, the quadrupolar Fano resonance and the dipole mode are observed more clearly.

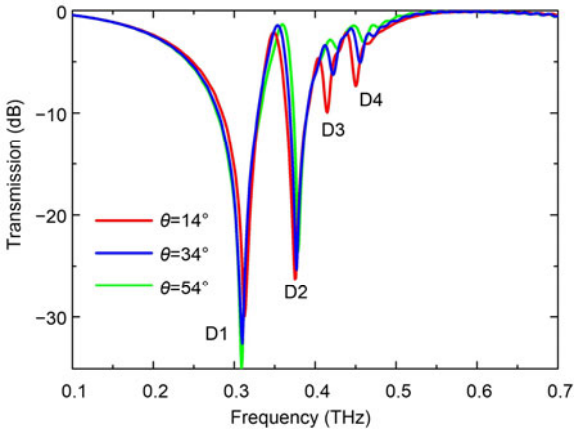

Fig. 23 Transmission spectra defective at angles 14°, 34°, and 54°

References to color refer to the online version of this figure

The quadrupole peaks in Fig. 22b have a characteristic of high Q, which can be used to fabricate a highly sensitive sensor (Cong et al., 2015). We choose the sharp quadrupolar peak and the higher dip on the resonance curve as two extreme points and then note the FWHM bandwidth (FWHM=Δf=f_2−f_1). Taking the ratio of the resonance frequency at peak, and the FWHM, i.e., f_0/Δf, we obtain the value for the Q factor. The key parameters of the Q-factor calculation of single defect structure are listed in Table 1.

Table 1 Key parameters for Q-factor calculation

θ (°)	f_0 (THz)	f_1 (THz)	f_2 (THz)	Δf (THz)	Q
6	0.387	0.382 50	0.391 60	0.009 10	42.527 47
8	0.383	0.377 90	0.387 84	0.009 94	38.531 19
10	0.380	0.374 80	0.385 30	0.010 50	36.190 48
12	0.377	0.371 80	0.382 85	0.011 05	34.117 65
14	0.374	0.368 40	0.379 90	0.011 50	32.521 74
16	0.375	0.368 90	0.380 30	0.011 40	32.894 74
18	0.375	0.368 90	0.380 30	0.011 40	32.894 74
20	0.375	0.369 05	0.380 70	0.011 65	32.188 84
22	0.376	0.370 00	0.381 50	0.011 50	32.695 65
24	0.376	0.370 30	0.381 84	0.011 54	32.582 32

Such a WG micro-cavity can also be excited in a planar chip using a high-efficiency coplanar waveguide (CPW) and a thin corrugated disk resonator (CDR) (Wang et al., 2017) (Fig. 24). The distance g, the width and the period of the groove a=0.5d, p=2πR/N (N=20), and the waveguide height h are also marked in Fig. 24. The sizes mentioned above are R=1200 μm, r=600 μm, h_1=500 μm, h_2=450 μm, and p=380 μm. To simulate the wave propagation in free space, a gold layer is modeled as a lossy metal and behaves almost like a perfect conductor in the THz range, and the quartz substrate is used as a loss material with dielectric loss tangent of tanδ=0.0004. The surface metal layer is 0.5-μm thick gold, and is fabricated by conventional lithography. To reduce the loss of this part, we can choose an excellent performance medium such as gallium arsenide, sapphire, or quartz as the substrate material. In this work, quartz is used as the substrate, of 200-μm thickness.

The simulated transmission coefficient (in dB) is displayed in Fig. 25a. The red curve is the plasmonic waveguide with CDR and the black curve shows the feature of the broadband transmission without a corrugated disk resonator. On the corrugated disk, the coupling of plasma waveguide and corrugated plate produces six main obliquities. Each dip corresponds to a different mode, which is marked in Fig. 25a (red curve). Figs. 25b–25g show the electric field (E_z) (0.1 mm above the metal film). Dips 1–6 in Fig. 25a correspond to resonance modes in Figs. 25b–25g. Dips 3–5 in the simulation band are quite obvious and have high Q factors. These three dips in Q factors are 44.6, 283.4, and 215.8. These can serve as good features for a biosensor. In the experiment, we focused mainly on these three high-Q dips (3–5).

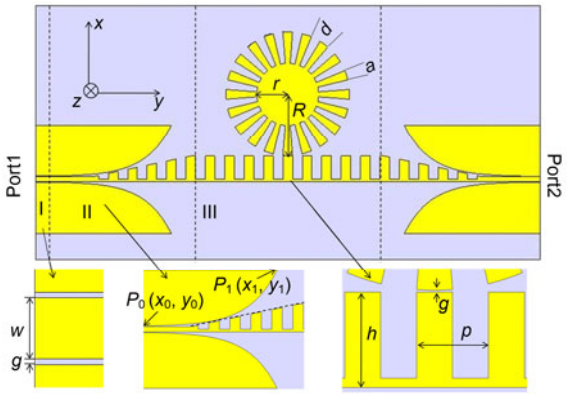

Fig. 24 Top view of a high Q plasma waveguide with a corrugated plate resonator system
The distance g, the width and the period of the groove a=0.5d, p=2πR/N (N=20), and the waveguide height h are also marked. The sizes mentioned above are R=1200 μm, r=600 μm, h_1=500 μm, h_2=450 μm, and p=380 μm. Reprinted from Wang et al. (2017), Copyright 2017, with permission from Springer Nature

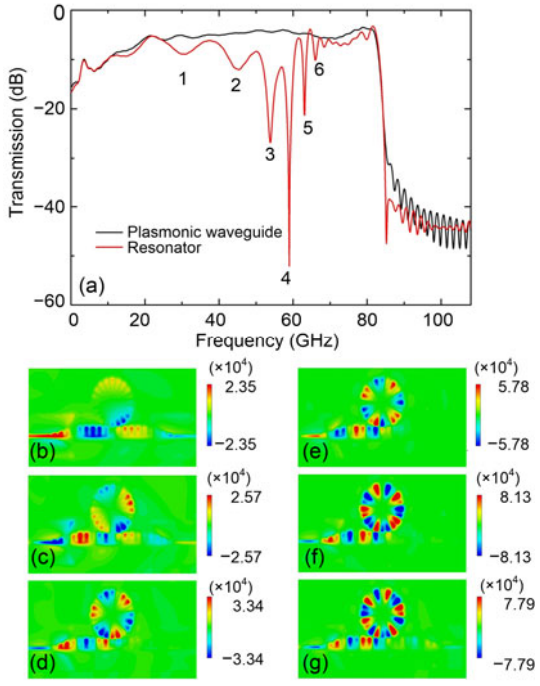

Fig. 25 (a) Transmission coefficients S_{21} of the biosensor system; (b–g) electric field (E_z) on an x-y plane which is 0.1 mm above the metal film
Dips 1–6 in (a) correspond to resonance modes in (b)–(g). References to color refer to the online version of this figure. Reprinted from Wang et al. (2017), Copyright 2017, with permission from Springer Nature

Next, we analyze the resonance frequencies of these dips (1–6). The phase change around the

corrugated disk is calculated as

$$\Delta\varphi = \beta 2\pi R = (2m+1)\pi. \tag{3}$$

Here β is the propagation constant. If we define $k=\beta/(2\pi/p)$ as the normalized wavenumber ($p=2\pi R/N$ is the periodic constant of CDR), Eq. (3) can be re-written as

$$k = \frac{\beta}{2\pi / p} = \frac{2m+1}{2R} \cdot \frac{p}{2\pi} = \frac{2m+1}{2N}. \tag{4}$$

When the disk is in the closed state, there is a relationship between k and m. This is shown in Table 2. The close state frequencies from dip 3 to 5 on parameter S_{21} and the frequencies from the corrugated disk dispersion curve are in agreement.

Table 2 Comparison of resonance frequencies

$k(2\pi/p)$	Frequency (GHz)	
	Theoretical	Simulation
0.175	53.8	53.8
0.225	60.1	59.0
0.275	64.2	63.2

Reprinted from Wang et al. (2017), Copyright 2017, with permission from Springer Nature

The biosensor system sample is displayed in Fig. 26. The size of quartz substrate is 15 mm×15 mm. The structure (CPW, waveguide and CDR) is processed by conventional lithography. A vector network analyzer (Agilent N5245A) with a frequency range from 50 to 75 GHz is used to measure the transmission coefficient. The probe pins are placed at ports 1 and 2, respectively. The experimental results (without detect material) are illuminated in Fig. 27. Modes 3–5 are observed clearly. In the experiment, the Q-value of the octupolar mode has been observed as high as 268.3. This high Q is suitable for an ultrasensitive sensor.

The corrugated disk resonances are sensitive to the change of surrounding materials. If the permittivity ε is changed within the corrugated disk grooves, all the resonance dips will shift. For the corrugated disk grooves filled with different refractive index materials, the resonance will be changed significantly. In our simulation, we obtain a 0.22 GHz shift in the hexapole and octupole resonance (from ε=1.02 to ε=1.1). In Fig. 28, when ε increases, the red-shift of the resonance dips moves to lower frequencies. Note that the sample is sensed by an evanescent field in this in-plane measurement.

The corrugated disk is an important part of the biological sensor system. We can fill different

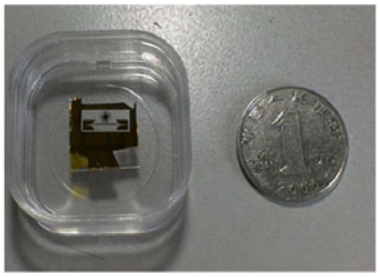

Fig. 26 Picture under a microscope
The parameter values are the same as in Fig. 24

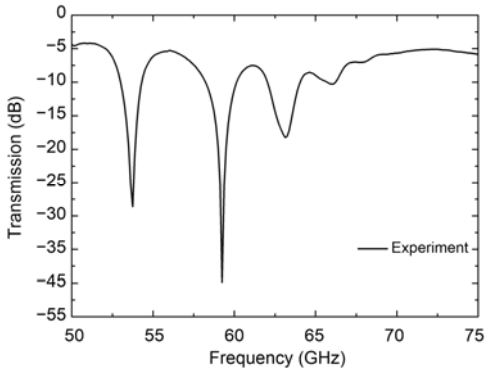

Fig. 27 Measured transmission coefficients S_{21} with CDR
Reprinted from Wang et al. (2017), Copyright 2017, with permission from Springer Nature

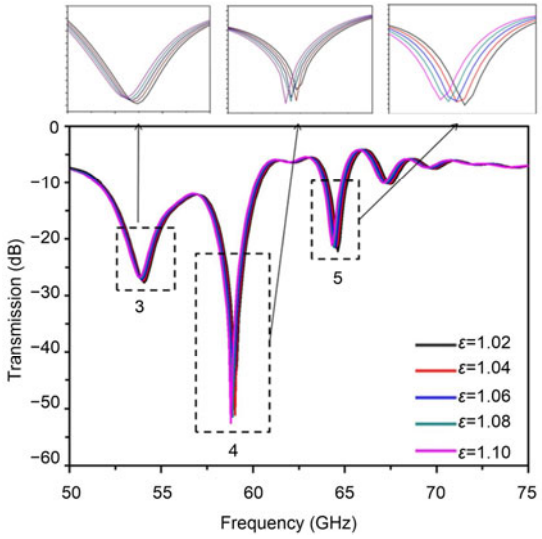

Fig. 28 Red-shift of the resonance dips
References to color refer to the online version of this figure

samples in the groove of the corrugated disk. Both solid and liquid can be measured. We choose different liquids in the experiment. We use a cotton swab dipped in liquid, and then cover the groove with liquid. When a liquid is replaced, the sensor sample is placed in the acetone and then in deionized water. A low power ultrasonic cleaning machine is used for cleaning. The fillers we used in experiments for filling the corrugated disk grooves are ethanol, deionized water, and olive oil. From Fig. 29, by filling different transparent liquids, unknown transparent liquids can be identified by measuring the resonance shift due to the refractive index changes with different fillers. We found that in addition to the red-shift, these dips' transmission coefficients (in dB) are also different. This may be due to the different influence of the electric field around the corrugated disk with different liquid concentration. We evaluate the sensitivity of the Fano-resonant structure in terms of Δf/(RIU/vol) when the sample is applied to the whole area or the CDR area only. For the refractive index of 1.17 (olive oil), the shift in the hexapole dip is 3.1 and 1.12 GHz in the two conditions, respectively. Here note that the volume of the analyte is much less in the second condition. To remove the influence of volume, we calculate the sensitivity per unit-volume. If the thickness of the sample is 5 μm, the resulting sensitivity is 0.0162 GHz/RIU/(mm^2×μm) when the whole chip is covered with the oil and 0.292 GHz/RIU/(mm^2×μm) in the case of the oil covering CDR only. The enhanced sensitivity is improved by a factor of 18. Note that our sensor size is small to avoid liquid overflow to the network analyzer probe, so that only a thin layer of liquid covers the groove. It may affect the actual dip offset of the sensor.

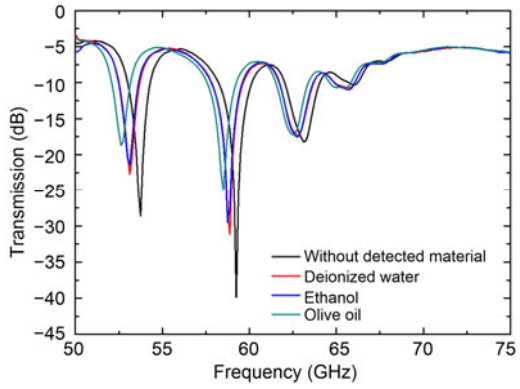

Fig. 29 Detection of different liquids in the corrugated disk groove

4 Conclusions

In this review, we briefly described the sample detection in the THz range. The method of THz spectroscopy can determine the unique absorption fingerprint spectrum and the complex refractive index of many materials using THz-TDS. However, the investigation of tiny sample volume has proven challenging due to weak power output of source, which can influence the SNR and further the material identification. To overcome these disadvantages, alternative approaches are required. In particular, high Q micro-cavity components/chips have been considered for samples with tiny volume (Xu et al., 2013b). We have listed three general micro-cavity components involving metallic photonics crystal, parallel plate waveguide, and plasmonic WG cavities, which represent metamaterial, guided wave, and resonant structures, respectively. Their performances are discussed in detail.

Characterization of materials in the THz range is a promising field. In recent years, an integrated microfluidic platform has been developed to detect real-time liquid sensing. It provides a possibility to monitor fast responses for many chemical and biological reactions (Liu et al., 2013). Moreover, a THz scattering near-field optical microscope has been used to investigate the characterization of two-dimensional materials, providing a unique tool for determining the properties of semiconductors and biomedical materials (Degl'Innocenti et al., 2017). The progress may help advance the current knowledge of sample detection with subwavelength THz science.

References

Auston DH, Cheung KP, Smith PR, 1984. Picosecond photoconducting Hertzian dipoles. *Appl Phys Lett*, 45(3):284-286. https://doi.org/10.1063/1.95174

Auston DN, Cheung KP, Valdmanis JA, et al., 1984. Cherenkov radiation from femtosecond optical pulses in electro-optic media. *Phys Rev Lett*, 53(16):1555-1558. https://doi.org/10.1103/PhysRevLett.53.1555

Bertero NM, Trasarti AF, Apesteguía CR, et al. 2011. Solvent effect in the liquid-phase hydrogenation of acetophenone over Ni/SiO_2: a comprehensive study of the phenomenon. *Appl Catal A*, 394(1-2):228-238. https://doi.org/10.1016/j.apcata.2011.01.003

Biber S, Hofmann A, Shulz R, et al., 2004. Design and measurement of a bandpass filter at 300 GHz based on a highly efficient binary grating. *IEEE Trans Microw Theory Tech*, 52(9):2183-2189.

https://doi.org/10.1109/TMTT.2004.834159

Bodrov SB, Stepanov AN, Bakunov MI, et al., 2009. Highly efficient optical-to-terahertz conversion in a sandwich structure with $LiNbO_3$ core. *Opt Expr*, 17(3):1871-1879. https://doi.org/10.1364/OE.17.001871

Carbajo S, Schulte J, Wu XJ, et al., 2015. Efficient narrowband terahertz generation in cryogenically cooled periodically poled lithium niobate. *Opt Lett*, 40(24):5762-5765. https://doi.org/10.1364/OL.40.005762

Chen L, Cao ZQ, Ou F, et al., 2007. Observation of large positive and negative lateral shifts of a reflected beam from symmetrical metal-cladding waveguides. *Opt Lett*, 32(11):1432-1434. https://doi.org/10.1364/OL.32.001432

Chen L, Zhu YM, Zang XF, et al., 2013a. Mode splitting transmission effect of surface wave excitation through a metal hole array. *Light Sci Appl*, 2(3):e60. https://doi.org/10.1038/lsa.2013.16

Chen L, Gao CM, Xu JM, et al., 2013b. Observation of electromagnetically induced transparency-like transmission in terahertz asymmetric waveguide-cavities systems. *Opt Lett*, 38(9):1379-1381. https://doi.org/10.1364/OL.38.001379

Chen L, Xu JM, Gao CM, et al., 2013c. Manipulating terahertz electromagnetic induced transparency through parallel plate waveguide cavities. *Appl Phys Lett*, 103(25):251105. https://doi.org/10.1063/1.4852115

Chen L, Truong KV, Cheng ZX, et al., 2014a. Characterization of photonic bands in metal photonic crystal slabs. *Opt Commun*, 333:232-236. https://doi.org/10.1016/j.optcom.2014.07.045

Chen L, Cheng ZX, Xu JM, et al., 2014b. Controllable multi-band terahertz notch filter based on a parallel plate waveguide with a single deep groove. *Opt Lett*, 39(15): 4541-4544. https://doi.org/10.1364/OL.39.004541

Chen L, Wei YM, Zang XF, et al., 2016. Excitation of dark multipolar plasmonic resonances at terahertz frequencies. *Sci Rep*, 6:22027. https://doi.org/10.1038/srep22027

Chen L, Xu NN, Singh L, et al., 2017. Defect-induced fano resonances in corrugated plasmonic metamaterials. *Adv Opt Mater*, 5(8):1600960. https://doi.org/10.1002/adom.201600960

Chen WQ, Peng Y, Jiang XK, et al., 2017. Isomers identification of 2-hydroxyglutarate acid disodium salt (2HG) by terahertz time-domain spectroscopy. *Sci Rep*, 7:12166. https://doi.org/10.1038/s41598-017-11527-z

Cong LQ, Manjappa M, Xu NN, et al., 2015. Fano resonances in terahertz metasurfaces: a figure of merit optimization. *Adv Opt Mater*, 3(11):1537-1543. https://doi.org/10.1002/adom.201500207

Consolino L, Taschin A, Bartolini P, et al., 2012. Phase-locking to a free-space terahertz comb for metrological-grade terahertz lasers. *Nat Commun*, 3:1040. https://doi.org/10.1038/ncomms2048

DeFonzo AP, Jarwala M, Lutz CR, 1987. Transient response of planar integrated optoelectronic antennas. *Appl Phys Lett*, 50(17):1155-1157. https://doi.org/10.1063/1.97947

Degl'Innocenti R, Wallis R, Wei BB, et al., 2017. Terahertz nanoscopy of plasmonic resonances with a quantum cascade laser. *ACS Photon*, 4(9):2150-2157. https://doi.org/10.1021/acsphotonics.7b00687

Dorney TD, Baraniuk RG, Mittleman DM, 2001. Material parameter estimation with terahertz time-domain spectroscopy. *J Opt Soc Am A*, 18(7):1562-1571. https://doi.org/10.1364/JOSAA.18.001562

Du SQ, Li H, Xie L, et al., 2012. Vibrational frequencies of anti-diabetic drug studied by terahertz time-domain spectroscopy. *Appl Phys Lett*, 100(14):143702. https://doi.org/10.1063/1.3700808

Ebbesen TW, Lezec HJ, Ghaemi HF, et al., 1998. Extraordinary optical transmission through sub-wavelength hole arrays. *Nature*, 391(12):667-669. https://doi.org/10.1038/35570

Fattinger C, Grischkowsky D, 1988. Point source terahertz optics. *Appl Phys Lett*, 53(16):1480-1482. https://doi.org/10.1063/1.99971

Federici J, Moeller L, 2010. Review of terahertz and sub-terahertz wireless communications. *J Appl Phys*, 107(11): 111101. https://doi.org/10.1063/1.3386413

Ferguson B, Zhang XC, 2002. Materials for terahertz science and technology. *Nat Mater*, 1:26-33. https://doi.org/10.1038/nmat708

Ferguson B, Wang SH, Gray D, et al., 2002. T-ray computed tomography. *Opt Lett*, 27(15):1312-1314. https://doi.org/10.1364/OL.27.001312

Ghaemi HF, Thio T, Grupp DE, et al., 1998. Surface plasmons enhance optical transmission through subwavelength holes. *Phys Rev B*, 58(11):6779-6782. https://doi.org/10.1103/PhysRevB.58.6779

Grischkowsky G, Keiding S, van Exter M, et al., 1990. Far-infrared time-domain spectroscopy with terahertz beams of dielectrics and semiconductors. *J Opt Soc Am B*, 7(10):2006-2015. https://doi.org/10.1364/JOSAB.7.002006

Hangyo M, Tani M, Nagashima T, 2006. Terahertz time-domain spectroscopy of solids: a review. *Int J Infr Millim Waves*, 26(12):1661-1690. https://doi.org/10.1007/s10762-005-0288-1

He JL, Liu PA, He YL, et al., 2012. Narrow bandpass tunable terahertz filter based on photonic crystal cavity. *Appl Opt*, 51(6):776-779. https://doi.org/10.1364/AO.51.000776

Huang Y, Min CJ, Veronis G, 2011. Subwavelength slow-light waveguides based on a plasmonic analogue of electromagnetically induced transparency. *Appl Phys Lett*, 99: 143117. https://doi.org/10.1063/1.3647951

Johnson C, Low FJ, Davidson AW, 1980. Germanium and germanium diamond bolometers operated at 4.2 K, 2.0 K, 1.2 K, 0.3 K, and 0.1 K. *Opt Eng*, 19(2):192255. https://doi.org/10.1117/12.7972503

Jones RC, 1947. The ultimate sensitivity of radiation detectors. *J Opt Soc Am*, 37(11):879-890. https://doi.org/10.1364/JOSA.37.000879

Katzenellenbogen N, Grischkowsky D, 1991. Efficient generation of 380 fs pulses of THz radiation by ultrafast laser pulse excitation of a biased metal-semiconductor interface. *Appl Phys Lett*, 58(3):222-224. https://doi.org/10.1063/1.104695

Leitenstorfer A, Hunsche S, Shah J, et al., 1999. Femtosecond charge transport in polar semiconductors. *Phys Rev Lett*, 82(25):5140-5143. https://doi.org/10.1103/PhysRevLett.82.5140

Leitenstorfer A, Hunsche S, Shah J, et al., 2000. Femtosecond high-field transport in compound semiconductors. *Phys Rev B*, 61(24):16642-16652. https://doi.org/10.1103/PhysRevB.61.16642

Libon IH, Baumgärtner S, Hempel M, et al., 2000. An optically controllable terahertz filter. *Appl Phys Lett*, 76(20):2821-2823. https://doi.org/10.1063/1.126484

Liu L, Pathak R, Cheng LJ, et al., 2013. Real-time frequency-domain terahertz sensing and imaging of isopropyl alcohol–water mixtures on a microfluidic chip. *Sens Actuat B*, 184:228-234. https://doi.org/10.1016/j.snb.2013.04.008

Lu T, Lee H, Chen T, et al., 2011. High sensitivity nanoparticle detection using optical microcavities. *Proc Nat Acad Sci USA*, 108(15):5976-5979. https://doi.org/10.1073/pnas.1017962108

Markelz AG, 2008. Terahertz dielectric sensitivity to biomolecular structure and function. *IEEE J Sel Top Quant Electron*, 14(1):180-190. https://doi.org/10.1109/JSTQE.2007.913424

Mendis R, Astley V, Liu JB, et al., 2009. Terahertz microfluidic sensor based on a parallel-plate waveguide resonant cavity. *Appl Phys Lett*, 95(17):171113. https://doi.org/10.1063/1.3251079

Miyamaru F, Hangyo M, 2004. Finite size effect of transmission property for metal hole arrays in subterahertz region. *Appl Phys Lett*, 84(15):2742-2744. https://doi.org/10.1063/1.1702125

Miyamaru F, Hayashi S, Otani C, et al., 2006. Terahertz surface-wave resonant sensor with a metal hole array. *Opt Lett*, 31(8):1118-1120. https://doi.org/10.1364/OL.31.001118

O'Hara JF, Singh R, Brener I, et al., 2008. Thin-film sensing with planar terahertz metamaterials: sensitivity and limitations. *Opt Expr*, 16(3):1786-1795. https://doi.org/10.1364/OE.16.001786

Planken PCM, Nienhuys HK, Bakker HJ, et al., 2001. Measurement and calculation of the orientation dependence of terahertz pulse detection in ZnTe. *J Opt Soc Am B*, 18(3):313-317. https://doi.org/10.1364/JOSAB.18.000313

Por A, Moreno E, Martin-Moreno L, et al., 2012. Localized spoof plasmons arise while texturing closed surfaces. *Phys Rev Lett*, 108(22):223905. https://doi.org/10.1103/PhysRevLett.108.223905

Pupeza I, Wilk R, Koch M, 2007. Highly accurate optical material parameter determination with THz time-domain spectroscopy. *Opt Expr*, 15(7):4335-4350. https://doi.org/10.1364/OE.15.004335

Qu DX, Grischkowsky D, Zhang WL, 2004. Terahertz transmission properties of thin, subwavelength metallic hole arrays. *Opt Lett*, 29(8):896-898. https://doi.org/10.1364/OL.29.000896

Shen XP, Cui TJ, 2014. Ultrathin plasmonic metamaterial for spoof localized surface plasmons. *Laser Photon Rev*, 8(1):137-145. https://doi.org/10.1002/lpor.201300144

Siegel PH, 2002. Terahertz technology. *IEEE Trans Microw Theory Tech*, 50(3):910-928. https://doi.org/10.1109/22.989974

Staus C, Kuech T, McCaughan L, 2008. Continuously phase-matched terahertz difference frequency generation in an embedded-waveguide structure supporting only fundamental modes. *Opt Expr*, 16(17):13296-13303. https://doi.org/10.1364/OE.16.013296

Su YY, 2014. Investigation of liquid monohydric alcohols by terahertz time-domain spectroscopy. *Opt Instrum*, 36(6):499-503 (in Chinese). https://doi.org/10.3969/j.issn.1005-5630.2014.06.007

Theuer M, Beigang R, Grischkowsky D, 2010a. Highly sensitive terahertz measurement of layer thickness using a two-cylinder waveguide sensor. *Appl Phys Lett*, 97(7):071106. https://doi.org/10.1063/1.3481080

Theuer M, Beigang R, Grischkowsky D, 2010b. Sensitivity increase for coating thickness determination using THz waveguides. *Opt Expr*, 18(11):11456-11463. https://doi.org/10.1364/OE.18.011456

Wang DN, Chen L, Fang B, et al., 2017. Spoof localized surface plasmons excited by plasmonic waveguide chip with corrugated disk resonator. *Plasmonics*, 12(4):947-952. https://doi.org/10.1007/s11468-016-0337-8

Wang YX, Zhang GW, Qiao LB, et al., 2014. Photocurrent response of carbon nanotube-metal heterojunctions in the terahertz range. *Opt Expr*, 22(5):5895-5903. https://doi.org/10.1364/OE.22.005895

Wang YX, Deng XQ, Zhang GW, et al., 2015. Terahertz photodetector based on double-walled carbon nanotube macrobundle-metal contacts. *Opt Expr*, 23(10):13348-13357. https://doi.org/10.1364/OE.23.013348

Withayachumnankul W, O'Hara JF, Cao W, et al., 2014. Limitation in thin-film sensing with transmission-mode terahertz time-domain spectroscopy. *Opt Expr*, 22(1):972-986. https://doi.org/10.1364/OE.22.000972

Wu DM, Fang N, Sun C, et al., 2003. Terahertz plasmonic high pass filter. *Appl Phys Lett*, 83(1):201-203. https://doi.org/10.1063/1.1591083

Wu Q, Zhang XC, 1997a. Free-space electro-optics sampling of mid-infrared pulses. *Appl Phys Lett*, 71(10):1285-1286. https://doi.org/10.1063/1.119873

Wu Q, Zhang XC, 1997b. 7 terahertz broadband GaP electro-optic sensor. *Appl Phys Lett*, 70(14):1784-1786. https://doi.org/10.1063/1.118691

Xu JM, Chen L, Xie L, et al., 2013a. Effect of boundary condition and periodical extension on transmission characteristics of terahertz filters with periodical hole array

structure fabricated on aluminum slab. *Plasmonics*, 8(3):1293-1297. https://doi.org/10.1007/s11468-013-9517-y

Xu JM, Chen L, Zang XF, et al., 2013b. Triple-channel terahertz filter based on mode coupling of cavities resonance system. *Appl Phys Lett*, 103(16):161116. https://doi.org/10.1063/1.4826456

Yomogida Y, Sato Y, Nozaki R, et al., 2010. Comparative dielectric study of monohydric alcohols with terahertz time-domain spectroscopy. *J Mol Struc*, 981(1-3):173-178. https://doi.org/10.1016/j.molstruc.2010.08.002

Zang XF, Shi C, Chen L, et al., 2015. Ultra-broadband terahertz absorption by exciting the orthogonal diffraction in dumbbell-shaped gratings. *Sci Rep*, 5:8901. https://doi.org/10.1038/srep08901

Zhao G, Schouten RN, van der Valk N, et al., 2002. Design and performance of a THz emission and detection setup based on a semi-insulating GaAs emitter. *Rev Sci Instrum*, 73(4):1715-1719. https://doi.org/10.1063/1.1459095

Zhu YM, Unuma T, Shibata K, et al., 2008a. Femtosecond acceleration of electrons under high electric fields in bulk GaAs investigated by time-domain terahertz spectroscopy. *Appl Phys Lett*, 93(4):042116-042118. https://doi.org/10.1063/1.2967857

Zhu YM, Unuma T, Shibata K, et al., 2008b. Power dissipation spectra and terahertz intervalley transfer gain in bulk GaAs under high electric fields. *Appl Phys Lett*, 93(23):232102. https://doi.org/10.1063/1.3039069